Journal of The Electrochemical Society, 2025 **172** 050528

Characterization of Cylindrical Lithium-Ion Batteries with Varying Electrolyte Amounts at Beginning of Life

Cara Zimmermann,[1,2,z] Camilla Tacconis,[2,3] Sophie Solchenbach,[2] Daniel Goldbach,[2] Simon Erhard,[2] Johannes Wandt,[2,4,z] and Simon Lux[1,5]

[1]*University of Münster, Institute of Business Administration at the Department of Chemistry and Pharmacy, Leonardo Campus 1, Münster, 48149, Germany*
[2]*Bayerische Motoren Werke Aktiengesellschaft (BMW AG), Petuelring 130, Munich, 80788, Germany*
[3]*University of Cambridge, Department of Physics, JJ Thomson Ave, Cambridge, CB3 0HE, United Kingdom*
[4]*University of Agder, Grimstad, 4879, Norway*
[5]*Fraunhofer Research Institution for Battery Cell Production FFB, Bergiusstraße 8, Münster, 48165, Germany*

This study investigates the impact of the electrolyte amount on the electrical performance at beginning of life in high energy cylindrical lithium-ion batteries. We investigate cylindrical 4695 prototype cells with varying pore filling ratios (PFRs), defined as the ratio of electrolyte volume to pore volume within anode, cathode, and separator. The PFR ranges from roughly half-filled pore volume to completely filled pore volume with additional free electrolyte. It is found that the energy and resistance remain constant as long as the PFR_{100} (at 100% SoC) > 1.00. As soon as the $PFR_{100} < 1.00$, the cell energy decreases, and the resistance increases with decreasing PFR. We also demonstrate the application of moment of inertia (MoI) measurements as a complementary technique to validate PFR calculations. Additionally, an analytical equation is developed to describe the relation between the electrolyte mass expelled from the jelly roll vs measured MoI change, isolating the contribution of electrolyte motion. This work lays the foundation for a subsequent study on the influence of PFR on the aging of cylindrical cells.
 [DOI: 10.1149/1945-7111/add438]

Manuscript submitted February 24, 2025; revised manuscript received April 8, 2025. Published May 19, 2025.

Supplementary material for this article is available online

For electric vehicles to compete with combustion engine vehicles, their driving range must be increased, which is directly related to the energy of the battery system. Additionally, the overall costs of electric vehicles must be reduced. One approach to tackle both challenges is to minimize the amount of electrolyte, as the electrolyte—in contrast to the active materials - does not directly contribute to the cell capacity.[1]

However, the electrolyte plays a crucial role within lithium-ion batteries. Its primary task is to enable the lithium-ion transport between anode and cathode by providing ionic conductivity through the separator, while simultaneously acting as an electrical insulator to prevent a short circuit between the anode and cathode. Furthermore, it is responsible for forming the solid electrolyte interface (SEI), a passivation layer at the anode, to ensure long service life of the battery. For optimal performance, it is crucial to ensure complete wetting of the electrodes and separator to maintain maximum ionic connection and thus to allow for complete de-/intercalation reactions of the active materials. Hence, an optimum must be found between weight and cost savings and full functionality of the cell over its entire service life.

Günter et al. investigated the influence of pore filling ratio (PFR) in graphite/layered nickel manganese cobalt oxide (NMC) pouch cells with a mean capacity of 3.2 Ah on electrical performance. The PFR is therein defined as the ratio of electrolyte volume to pore volume within anode, cathode, and separator before formation at 0% state of charge (SoC), and cells with PFR ranging from 0.6 to 1.8 were analyzed. Electrochemical impedance spectroscopy (EIS) was used to analyze the high frequency resistance (HFR), which represents the real part of the impedance at which the imaginary part is zero, corresponding to the point where the impedance exhibits a zero-crossing in a Nyquist plot. They measured the lowest HFR at a PFR $\geqslant$ 1.4. As the PFR decreased, the HFR increased, ranging between 6 mΩ to 20 mΩ. Additionally, the C/2 specific capacity ranged from roughly 125 mAh g^{-1} to 145 mAh g^{-1} at the beginning of life (BOL) whereby the maximum was reached at a PFR $\geqslant$ 1.4.[2]

An et al. analyzed the interplay of PFR on electrochemical performance in Si-graphite/NMC pouch cells with a capacity of 100 mAh, tested under 0.1 kg cm^{-2} external pressure. A high PFR range of 1.6 to 3.5 was investigated, with the 10 s resistances at ~3.6 V ranging from approximately 30 Ωcm^2 to 65 Ωcm^2 at BOL. The lowest resistance was observed at a PFR $\geqslant$ 2.1. The C/2 specific capacity normalized to the cathode mass ranged from 85 mAh g^{-1} to 135 mAh g^{-1} at BOL with a maximum value at a PFR $\geqslant$ 2.1, accounting for fluctuations between individual cells.[3] Both studies show a great dependency of resistance and capacity on the PFR, with better performance at high electrolyte amounts. However, the optimal PFR for the best electric performance is dependent on the cell's form factor, as the void volume varies strongly among different cell formats.[4]

For commercially available cells, the PFR is difficult to specify, as both the electrolyte amount and the pore volume are typically not given. Further, the PFR changes over the lifetime of a LIB. Gauthier et al. found that during the aging of a 220 mAh NMC622/Gr pouch cell, the positive electrode thickness increased, leading to a larger pore volume.[5] This increase in pore volume over the aging process is dependent on the cell's geometric constrains, as the mechanical forces imposed by the cell housing vary across different cell formats. Additionally, electrolyte is consumed by side reactions over the cell's lifetime.[6–11] The combination of these two effects causes a decrease in PFR during aging, which can result in electrolyte depletion within the cell, leading to a rapid drop in capacity over a short period of time.[12]

Hence, it is important to experimentally determine the PFR over the lifetime by measuring both the electrolyte quantity and pore volume. Yet, it is a non-trivial task to precisely determine the amount of electrolyte in a Li-ion cell. For pouch cells, various methods have been explored in the literature to investigate the electrolyte amounts. Petibon et al. quantified the residual amount of additives at different states of charge during formation by liquid-liquid extraction and subsequent gas chromatography coupled with mass spectroscopy,[13] while Thompson et al. extracted small amounts of electrolyte using a centrifuge.[10] The method was further improved to quantify at least 93% of the absolute amount of electrolyte

[z]E-mail: cara.zimmermann@bmw.de; johannes.wandt@bmw.de

components by injecting diethyl carbonate into the cell by Stockhausen et al.[14] The wetting degree of lithium-ion pouch cells was visually accessed non-destructively by ultrasonic scanning by Deng et al.[15]

In contrast to the above presented studies on pouch cells, quantifying the electrolyte volume and its distribution within cylindrical lithium-ion cells remains a significant challenge. Schoenemeier et al. introduced a liquid-liquid extraction technique capable of recovering 83% of conductive salts and up to 89% of solvents from cells, providing a benchmark for electrolyte analysis in cylindrical cells.[16] The major challenge for cylindrical cells is that most of the electrolyte resides within the highly compressed pore network of the jelly roll. The resolution of CT-imaging is insufficient to resolve wet regions or accurately quantify electrolyte volume within such small pore networks. While CT-scans are effective for visualizing electrolyte outside the compressed jelly roll,[16–18] no experimental method currently provides the precision required to differentiate between subtle variations in electrolyte volume or precisely determine the PFR.

In a seminal paper, Aiken et al. published a novel method to analyze the electrolyte motion within a cylindrical cell as a function of its SoC.[18] This method uses the non-destructive operando probe of the moment of inertia (MoI) of a cylindrical cell to study the flow of electrolyte towards the terminal end during charge and discharge. Solchenbach et al. were the first to use this method to distinguish between a lithium-ion cell with high and low electrolyte amounts.[17] The present study advances the use of MoI by proposing a simplified theoretical model that quantifies the mass of electrolyte expelled from the jelly roll during charging. We also highlight the potential of MoI measurements to accurately identify the critical inflection point where PFR $>$ 1.00 occurs in cells with varying electrolyte filling.

This work addresses two main objectives. First, we focus on the electric performance of prototype 4695 cylindrical lithium-ion cells with varying PFRs. Second, we present a theoretical model for the analysis of MoI measurements, enabling the determination of electrolyte mass moved out of the jelly roll as a function of SoC. We further show that trends in MoI measurements effectively distinguish between cells with PFR $>$ 1.00 and PFR $<$ 1.00. This study is part one of a two-part investigation, where we present a detailed analysis of BoL cells. In a later study, the tools developed in this work will be used to present a comparison of BoL with aged cells and analyze the influence of electrolyte amount on long-term cell performance.

Experimental

Investigated cells.—Cylindrical 4695 lithium-ion cells produced at BMW facilities are investigated. The cells are produced at a prototype production line for research and development purposes and are not used in any vehicle project. Due to confidentiality reasons, not all design parameters can be provided in full detail. Hence approximate values indicated by "∼" are given, and normalizations are used. The investigated cells are designed for high-energy purpose with an energy density of ∼800 Wh l^{-1}, specific energy of ∼300 Wh kg^{-1} and reversible areal capacity of ∼4 mAh cm^{-2}. The anode areal capacity exceeds the cathodic areal capacity by ∼5%, resulting in a N/P-ratio of ∼1.05. The jelly roll is connected to the steel can by so called "continuous tabbing" similar to Ref. 19. The anode active material consists of a mixture of graphite and a small amount of silicon carbon composite Si/C ($<$ 10 weight-%). NMC with a high nickel content $>$ 85 atomic-% is used as cathode active material. The electrolyte consists of the linear and cyclic carbonates ethylene carbonate, dimethyl carbonate, ethyl methyl carbonate and fluoroethylene carbonate, 1.2 M $LiPF_6$ conductive salt and additives, with a density of 1.26 g cm^{-3}.

Cells with eight distinct electrolyte amounts are analyzed as shown in Table I. Their electrolyte quantity ranges from 0.89 g Ah_{theor}^{-1} to 1.50 g Ah_{theor}^{-1}. The electrolyte quantity is expressed as the ratio of the filled electrolyte amount (g) to the theoretical available capacity of the cell (Ah_{theor}). The electrolyte amount is precisely filled during production with a maximum deviation of 0.01 g Ah_{theor}^{-1} or smaller. Depending on the electrolyte quantity a minimum of 2 cells are produced as shown in Table I. The cells are produced in two different batches. Batch 1 consists of four different electrolyte amounts, all of which have an electrolyte quantity $<$ 1.3 g Ah_{theor}^{-1} and batch 2 consists of the remaining four electrolyte amounts, all of which have an electrolyte quantity $>$ 1.3. Batch 1 and batch 2 were produced according to the same design. However, batch 1 was manufactured at a different time, leading to slight variations in e.g. porosity, loading density, electrode thickness and length.

Computer tomography.—CT-scans are performed on one exemplary cell of each electrolyte filling quantity at 0% and 100% SoC to investigate the location of the free electrolyte and the jelly roll dimensions. The scans are recorded at 25 °C with a Phoenix V|tome| x M (Waygate Technologies) with 250 kV voltage, 260 μA cathode current, 2900 images per scan and 36 μm voxel size. The cell is positioned upright with terminal at the top during the scan. Prior to the measurement the cell is discharged/charged to 0% SoC/100% SoC with CCCV of C/3 until 2.8 V/4.2 V and I $<$ C/50.

Electrochemical characterization.—All cells are electrically characterized during an initial check-up at 25 °C as shown in Table II. The C-rate always refers to the theoretical capacity and is consequently the same for all cells. The check-up starts with the capacity/energy check comprised of three cycles (steps 1–7) consisting of a C/3 constant current (CC) charge to 4.2 V, a constant voltage (CV) phase at 4.2 V with a current cutoff at C/50, and a C/3 CC discharge until 2.8 V. The capacity and energy are determined from the third CC discharge step. In a fourth cycle (steps 8–11), with the same charge protocol, the discharge rate capability is tested by applying a CC discharge of 1 C to 2.8 V.

In the next section the resistance is determined by EIS and pulse measurements. Galvanostatic EIS is performed at 100% SoC, 50% SoC and 0% SoC (steps 12–20) with an excitation amplitude of 0.3 A, containing 32 frequency measurement points in logarithmic spacing between 10 mHz and 10 kHz. First, the cell is charged with CCCV until 4.2 V and I $<$ C/50 followed by a rest period of 180 min. Subsequently the EIS at 100% SoC is performed. Afterwards, the cell is discharged with a CC of C/3 to 50% SoC, whereby the charge throughput is controlled by coulomb counting. The SoC refers to the actual capacity determined from steps 1–7. After a 180-minute rest period the EIS at 50% SoC is performed. In the end the EIS at 0% SoC is measured by previously discharging the cell with CCCV until 2.8 V and I $<$ C/50 and letting it rest for 180 min.

The pulse resistance is determined every 2% ΔSoC in charge and discharge directions (steps 21–30). Therefore, the cell is first discharged to 0% SoC CCCV until 2.8 V and I $<$ C/50. Afterwards the cell is charged with a CC of C/3 until a charge throughput of 2% ΔSoC is reached, controlled by coulomb counting, followed by a 2 min rest period. The pulse resistance is determined by analyzing the voltage drop after 0.1, 1.0 and 10.0 s during the rest period. This is repeated until 4.2 V and I $<$ C/50 is reached. To determine the discharge pulse resistance, the voltage rise during the rest period is analyzed with the same procedure in discharge direction until 2.8 V and I $<$ C/50. The rest period is analyzed instead of the current pulse to prevent OCV changes during resistance determination.

In the final step the capacity and energy are measured with a comparable low current rate of C/20 CC in charge and discharge direction (steps 31–38). This measurement is used as pseudo-open circuit voltage (pOCV) to perform differential voltage analysis (DVA).

During the check-up the cell temperature is measured by Type "K" (NiCr-Ni) and NTC 5 kOhm (Epcos B57861-S502-F40) sensors with a temperature uncertainty of ±1 K positioned at the outer cell

Table I. Electrolyte quantity and number of investigated cells.

		Batch 1				Batch 2			
electrolyte quantity	g/Ah_{theor}	0.89	1.00	1.11	1.22	1.34	1.39	1.45	1.50
max deviation	g/Ah_{theor}	0.00	0.00	0.01	0.01	0.01	0.01	0.01	0.01
number of cells	—	3	2	3	3	3	4	3	4

Table II. Check-up protocol at 25 °C.

	Nr	Step
Capacity/Energy Check	1	CC discharge with C/3 to 2.8 V
	2	Rest 30 min
	3	CCCV charge with C/3 to 4.2 V and I < C/50
	4	Rest 30 min
	5	CC discharge with C/3 to 2.8 V
	6	Rest 30 min
	7	Repeat step 3–6 3x (=3 cycles, 3rd discharge is used to determine capacity/energy)
	8	Rest 10 min
	9	CCCV charge with C/3 to 4.2 V and I < C/50
	10	Rest 30 min
	11	CC discharge with 1 C to 2.8 V
EIS	12	CCCV charge with C/3 to 4.2 V and I < C/50
	13	Rest 180 min
	14	Galvanostatic EIS (amplitude: 0.3 A; frequency range:10 mHz—10 kHz)
	15	CC discharge with C/3 to 50% SoC by coulomb counting
	16	Rest 180 min
	17	Galvanostatic EIS (amplitude: 0.3 A; frequency range:10 mHz—10 kHz)
	18	CCCV discharge with C/3 to 2.8 V and I < C/50
	19	Rest 180 min
	20	Galvanostatic EIS (amplitude: 0.3 A; frequency range:10 mHz—10 kHz)
Pulse resistance	21	Rest 10 min
	22	CCCV discharge with C/3 to 2.8 V and I < C/50
	23	Rest 30 min
	24	CC charge with C/3 until 2% ΔSoC, if 4.2 V is reached CV until I < C/50
	25	Rest 2 min
	26	Repeat step 24–25 until 100% SoC (4.2 V CCCV)
	27	Rest 30 min
	28	CC discharge with C/3 for 2% ΔSoC, if 2.8 V is reached CV until I < C/50
	29	Rest 2 min
	30	Repeat step 28–29 until 0% SoC (2.8 V CCCV)
pOCV	31	Rest 10 min
	32	CCCV discharge with C/3 to 2.8 V and I < C/50
	33	Rest 30 min
	34	CC charge with C/20 until 4.2 V
	35	Rest 10 min
	36	CCCV charge with C/3 to 4.2 V and I < C/50
	37	Rest 30 min
	38	CCCV discharge with C/20 until 4.2 V and I < C/50

can in the middle of the cell height. The capacity/energy check and the EIS measurement are performed with a multiple cell tester Digatron HD 40 A (MCT 40-6-32(16) HD, Digatron Power Electronics GmbH, Germany) and Digatron RE 300 A (MCT 250-06-18 RE, Digatron Power Electronics GmbH, Germany) system with current uncertainty of ±20 mA/±250 mA and voltage uncertainty of ±3 mV/±3 mV, respectively. The pulse resistance and the pOCV are determined with a high-resolution battery tester HPT 50 A (HRT-L50, Battery Dynamics GmbH, Germany) and HPT 150 A (HRT-L150, Battery Dynamics GmbH, Germany) with current uncertainty of ±5 mA/±15 mA and voltage uncertainty of ±0.6 mV/±0.25 mV, respectively. The complete check-up is performed in a temperature chamber TempEvent T/340/40/3/S (Weiss Technik GmbH, Germany) and KB 720 (E6) (BINDER GmbH, Germany) with temporal temperature uncertainty of ±0.1 K to ±0.5 K and spatial temperature uncertainty of ±0.2 K to ±1.0 K at Capgemini Deutschland GmbH, Germany.

Pore filling ratio.—The pore filling ratio (PFR) is a metric to describe the amount of electrolyte present within the cell. It is defined as the ratio of the volume of electrolyte ($V_{electrolyte}$) present in the cell to the total pore volume (V_{pore}) within the jelly roll.

$$\mathrm{PFR\ (SoC)} = \frac{V_{\mathrm{electrolyte}}}{V_{\mathrm{pore}}\,(\mathrm{SoC})} \quad [1]$$

The pore volume of the jelly roll V_{pore} includes the porosity of the anode, cathode and separator.

The PFR in this paper is calculated analogously as described by Solchenbach et al.[17] The $V_{\mathrm{electrolyte}}$ used in the PFR calculation is the electrolyte volume present in the BoL cell after formation, accounting for the fraction of electrolyte consumed in SEI formation. The V_{pore} (SoC) is determined by measuring the effective volume occupied by the jelly roll within the cell $V_{\mathrm{jelly\ roll}}$ (SoC) and subtracting the total volume occupied by the solid material forming the jelly roll (both active and inactive) after formation.

$$V_{\mathrm{pore}}\,(\mathrm{SoC}) = V_{\mathrm{jelly\ roll}}\,(\mathrm{SoC}) - V_{\mathrm{material}}\,(\mathrm{SoC}) \quad [2]$$

In this study V_{material} (SoC) is calculated using a complex model that was first introduced in Ref. 17. Within this model, V_{material} (SoC), and consequently also the V_{pore} (SoC), always refers to values after formation, taking into consideration SEI volume and initial irreversible jelly roll expansion.[20,21] Further, the model includes the SoC dependency of these quantities, which arises as the active material within the cell expands and contracts as a function of its lithiation state. To calculate $V_{\mathrm{jelly\ roll}}$ (SoC) the total jelly roll dimensions are determined by CT-scans, as discussed in detail in the results section. As discussed later, we assume that our pore filling calculation is correct within ± 0.05.

Our model differs from the PFR definitions presented so far by Günter et al.[2] and An et al.,[3] which refer to the SoC-independent PFR prior to formation.

The PFR can give useful information into the expected distribution of the electrolyte throughout the cell. For example, with a PFR = 1, we would expect all the electrolyte to be stored in the jelly roll and completely fill all the jelly roll pore volume. A PFR $>$ 1 can be visualized as a scenario in which all the pore volume within the jelly roll is filled with electrolyte, with the excess electrolyte overflowing from the jelly roll into other components of the battery. In this study, we will refer to this excess electrolyte outside the jelly roll as "free electrolyte," which can be located in the mandrel (hollow core of the jelly roll) or the donut volume (separator and current collector overhang at the top/bottom of the jelly roll, see Fig. 7 and related discussion).[9,17,22,23] Finally, a PFR $<$ 1 signifies there is not enough electrolyte within the cell to fully fill the entire pore volume in the jelly roll. Determining how this last scenario would look within a cylindrical cell is complicated, as the distribution of the electrolyte in such cases has not been studied and may change with cycling. As briefly touched upon in the supporting information of Ref., 17 this could either be interpreted as partial drying of sections of the jelly roll, with others having fully filled pores, or in the opposite case with an equal filling level of all pores, where both gas and electrolyte are equally distributed in the pores (see supporting information Fig. S1).

Finally, Solchenbach et al.[17] showed how theoretically the PFR of a cylindrical cell evolves with its SoC. As the cell is charged, the silicon and graphite lithiation occurs, which is accompanied by a large volume increase at the anode. The anode active material expansion reduces the anode porosity, while $V_{\mathrm{electrolyte}}$ remains constant, resulting in an increase of PFR at 100% SoC (denoted as PFR_{100} in this study) compared to PFR at 0% SoC (denoted as PFR_0).[24–29] As the cell discharges, anode delithiation occurs, and the pore volume of the anode is expected to return to a value close to its original, meaning the PFR approaches the lower value of PFR_0. For cells with $\mathrm{PFR}_{100} \geqslant 1$, electrolyte is pushed out of the jelly roll during charging, producing free electrolyte. As the cell discharges, the electrolyte pushed out can be pulled back into the jelly roll by capillary forces.[9,23]

Moment of inertia.—In this work, the MoI is experimentally measured for each cell using the air-bearing pendulum Resonic T from Resonic GmbH, Berlin, Germany. The same setup is used as in Ref. 17.

The experiment measures the resonant frequency of a cylindrical cell mounted on a torsional oscillator. To determine the oscillation frequency, a pulse is applied to the oscillator, and 10 oscillation cycles are measured. The frequency measurement is repeated 10 times with independent pulses applied in intervals of 18 s. After approximately half an hour the procedure is repeated to account for possible fluctuations over time. The mean frequency obtained from the 20 individual pulses is set as the oscillation frequency (f) of the cell at a given SoC. Using Eq. 3 the MoI I of the cylindrical cell is calculated.[30]

$$f = \frac{1}{2}\pi\sqrt{\frac{k}{I}} \quad [3]$$

where k is the spring constant which is determined by the calibration at the beginning of each experiment.

The MoI is investigated at 0% SoC and 100% SoC. First the cell is discharged to 0% SoC with a CCCV profile of C/5 until 2.8 V and current $<$ C/50, followed by a storage period for at least half a day to ensure an even electrolyte distribution. Right before the MoI measurement, the cell is once more discharged with the same profile to 0% SoC. After the measurement, the cell is charged to 100% SoC with CCCV of C/5 until 4.2 V and I $<$ C/50. The MoI at 100% SoC is performed directly after the end of charge.

Results

CT-scan.—Figure 1 shows CT-scans of an exemplary 4695 cell with the highest investigated electrolyte quantity (1.50 g $\mathrm{Ah_{theor}}^{-1}$). For those cells, we expect excess electrolyte to be pushed out of the jelly roll and into the other cell components at 100% SoC. The greyscale indicates the density of the material, where a high density corresponds to a brighter value. If there is free electrolyte located outside the jelly roll, this area appears correspondingly brighter than if the area were empty. To better visualize the free electrolyte, its corresponding greyscale values are colored in blue. As the grayscale values of the electrolyte may vary slightly and overlap with other cell components, this color coding may not capture all the free electrolyte present.

Figures 1a and 1b show the vertical cross-section of the upper region of the cylindrical cell at (a) 0% SoC and (b) 100% SoC. At 0% SoC no free electrolyte is visible, whereas at 100% SoC free electrolyte (depicted in blue) is present right above the jelly roll in the empty space between the current collector and separator overhang. The height of the free electrolyte is measured by CT-scans and corresponds to approximately 1/3 of the height of the donut volume.

Additionally, small quantities of electrolyte are attached to the separator in the void mandrel volume. However, the majority of the free electrolyte is located in the upper donut volume, as evident from the vertical cross-section of the entire cell at 100% SoC in Fig. 1c. No free electrolyte is visible in the lower donut volume, most likely due to the cell being stored upside down prior to the scan. This behavior differs from the previously published CT-scans from Bond et al.[23] of 18650 cells with a large excess of free electrolyte, which showed significant amounts of free electrolyte within the mandrel volume. An 18650 cell has an empty volume of ∼400 µl in the donut region (bottom and top) and ∼460 µl in the mandrel volume.[23] By contrast, in the investigated 4695 cells, there is an empty volume of ∼8.5 ml in the donut region (bottom and top), while the mandrel volume only accounts to ∼1.5 ml.[17] Hence, the ratio of void donut volume to void mandrel volume in an 18650 cell (∼0.87) is significantly lower than in an 4695 cell (∼5.67). Therefore, free electrolyte inside the mandrel is much more common in an 18650 cell. CT-scans of the remaining cells with lower electrolyte quantities were also performed at 0% SoC and 100% SoC, which

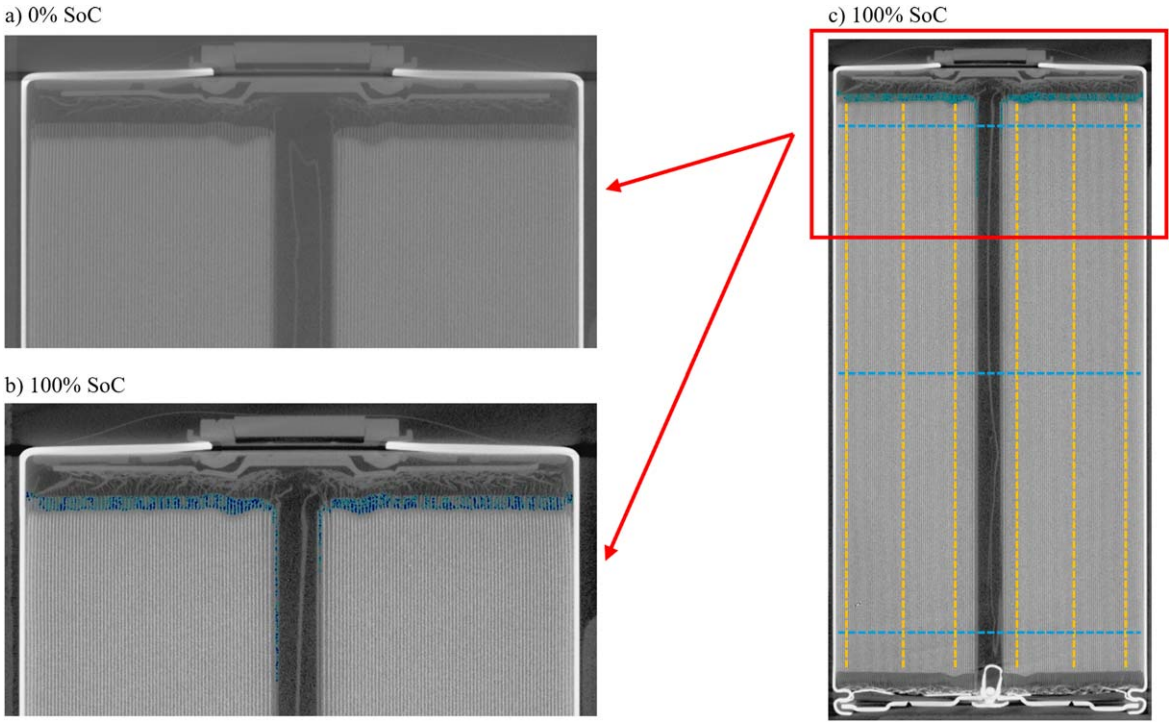

Figure 1. CT-images of an exemplary 4695 cell with the highest investigated electrolyte quantity (1.50 g Ah_{theor}^{-1}). Free electrolyte, located outside the jelly roll, is visualized in blue. Vertical cross-section of the upper region of the cell, depicting the upper jelly roll and donut volume at (a) 0% SoC and (b) 100% SoC. (c) Vertical cross-section of the entire cell at 100% SoC; the red box represents the region of image (a) and (b); horizontal blue dashed lines represent the area in which the jelly roll outer radius and mandrel radius are evaluated; vertical yellow dashed lines represent the area in which the height of the jelly roll is extracted.

Table III. Jelly roll dimension at 0% SoC and 100% SoC.

Batch 1			
0% SoC		100% SoC	
R_0	100.00%	R_{100}	100.10%
r_0	100.00%	r_{100}	99.41%
L_0	100.00%	L_{100}	100.14%
Batch 2			
0% SoC		100% SoC	
R_0	100.00%	R_{100}	100.08%
r_0	100.00%	r_{100}	97.94%
L_0	100.00%	L_{100}	100.42%

all reveal no electrolyte inside the donut volume nor the mandrel volume and are therefore not shown. The results of the CT-scans confirm that nearly no electrolyte overflow into the mandrel volume is occurring, and thus that our MoI analysis model can be applied to all cells in this study.

Further, we investigate the jelly roll dimensions at 0% SoC and 100% SoC by CT-scans. The outer radius R_0 and R_{100} of the jelly roll and the radius of the mandrel r_0 and r_{100}, both measured from the center of the cell, at 0% SoC and 100% SoC, respectively, are measured three times, each at the top middle and bottom of the jelly roll, as indicated by the horizontal light blue dashed lines in Fig. 1c. The jelly roll length L_0 and L_{100} at 0% SoC and 100% SoC, respectively, are measured each in total 6 times at various jelly roll positions, as indicated by the vertical yellow dashed lines in Fig. 1c. The dimensions of the jelly roll, *R, r,* and *L* are visualized in the schematic illustration of the jelly roll shown in Fig. 7 in the subsequent results of the MoI. The measured mean jelly roll dimensions at 0% SoC and 100% SoC are shown in Table III. The values are normalized to the respective value at 0% SoC. Cells from batch 1 and batch 2 reveal significantly different mean expansions, which might be attributed to varying electrode lengths in the jelly roll. Variations within cells of the same batch is less significant than the average change in production lengths between batches 1 and 2.

Hence, the mean expansion of batch 1 cells and batch 2 cells are separately listed. During charge, the jelly roll radius and its length expand by 0.11% and 0.14% for batch 1 and 0.08% and 0.42% for batch 2, whereas the mandrel radius shrinks by 0.59% for batch 1 and 2.06% for batch 2. This can be attributed to an overall expansion of the full cells active materials at 100% SoC,[17] resulting in a net expansion of the jelly roll in the radial and longitudinal direction.

The effective jelly roll volume $V_{\text{jelly roll}}$ (SoC) used in the PFR calculations, as seen in Eq. 2, is calculated using the formula of a hollow cylinder, $V = \pi \cdot (R^2 - r^2) \cdot L$. It increases by 0.32% for batch 1

Table IV. SoC dependent pore filling ratios calculated for the cylindrical cells in this study and filled electrolyte quantity.

		Batch 1				Batch 2			
electrolyte quantity	g/Ah_{theor}	0.89	1.00	1.11	1.22	1.34	1.39	1.45	1.50
PFR at 100% SoC	—	0.62	0.73	0.80	0.90	1.00	1.04	1.08	1.12
PFR at 50% SoC	—	0.61	0.70	0.78	0.87	0.97	1.01	1.05	1.08
PFR at 0% SoC	—	0.55	0.64	0.71	0.79	0.88	0.91	0.95	0.98
max deviation	—	0.00	0.00	0.00	0.01	0.01	0.01	0.01	0.01

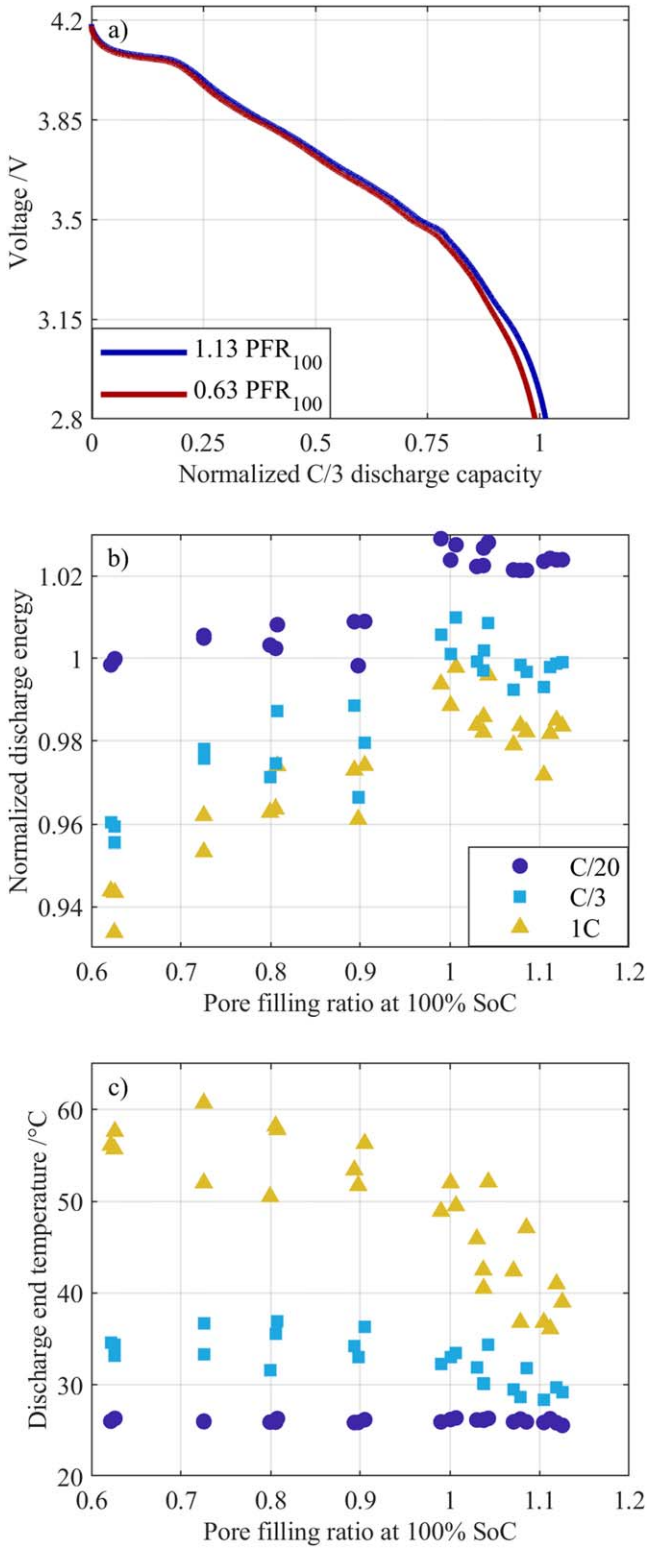

Figure 2. (a) Voltage vs discharge capacity measured with C/20 of the highest (1.13) and lowest (0.62) investigated PFR_{100}, shown in blue and red, respectively. (b) Constant current discharge energy and (c) cell can temperature at the end of the constant current discharge plotted against PFR_{100}. C-rates of C/20, C/3 and 1 C are depicted in dark blue circles, bright blue squares, and yellow triangles, respectively. The energy and capacity are normalized by the mean of all energies and capacities, respectively, measured with C/3 and $PFR_{100} > 1$.

and 0.54% for batch 2 while charging the cell from 0% SoC to 100% SoC.

Calculated pore filling ratio.—The jelly roll volume expansion, measured by CT-scans, was implemented in the PFR calculation, to obtain the theoretical PFR of the investigated cells, shown in Table IV. The maximum deviation of the PFR within a group of electrolyte quantities is less than or equal to 0.01. All cells have a PFR < 1.00 at 0% SoC (PFR_0) ranging from roughly half-filled pore volume (0.55 PFR_0) to nearly fully filled pore volume (0.98 PFR_0). These PFRs align well with the previously examined CT-scans, in which no free electrolyte was found at 0% SoC. At 50% SoC the PFR (PFR_{50}) ranges from 0.61 PFR_{50} to 1.08 PFR_{50}. At 100% SoC the PFR (PFR_{100}) of batch 1 is significantly below 1.00 ranging from 0.62 PFR_{100} to 0.90 PFR_{100}, whereas all cells of batch 2 have a PFR $\geqslant 1.00$, ranging from 1.00–1.12 PFR_{100}. In contrast, free electrolyte was only observed in the CT-scans for the highest PFR. This could show the limitations of CT-scans in tracking small amounts of free electrolyte.

Energy and capacity.—Figure 2a displays the voltage vs capacity profiles for constant-current (CC) discharges performed at a rate of C/20 for the highest investigated PFR_{100} value (1.12, shown in blue) and the lowest investigated PFR_{100} value (0.62, shown in red). The capacity values have been normalized to the average capacity of all cells with $PFR_{100} > 1.00$ discharged under identical C/3 CC conditions. The capacity of the low PFR cell is 2.4% less than the high PFR cell. Further, the mean voltage of the low PFR cell (3.685 V) is nearly identical to the mean voltage of the high PFR cell equal to 3.689 V.

The relationship between energy and PFR_{100} of the investigated cells is shown in Fig. 2b. The energy is measured with a constant discharge current of C/20, C/3 and 1 C depicted by dark blue circles, bright blue squares, and yellow triangles, respectively. The energies are normalized by the mean energy of all cells with a $PFR_{100} > 1.00$ at C/3 CC. For cells with $PFR_{100} > 1.00$, the C/3 discharge energy is distributed around a mean value, with the observed spread likely attributable to production-related fluctuations. At the transition from $PFR_{100} > 1.00$ to $PFR_{100} < 1.00$, a distinct decrease in energy is observed, which may reflect production differences between the two batches. Beyond this transition, the energy decreases exponentially with decreasing PFR_{100}. In total, the C/3 discharge energy reduces by 4.3% from $PFR_{100} > 1.00$ to $PFR_{100} = 0.62$, indicating a relatively minor energy loss. The C/20 measured energy shows a similar PFR_{100} dependency as the C/3 energy but shifted towards higher values, with a smaller energy reduction of 2.5% over the investigated PFR range. The 1 C energy shows also a comparable PFR_{100} dependency but shifted towards lower values, with an overall reduction of 4.8% from $PFR_{100} > 1.00$ to $PFR_{100} = 0.62$.

Figure 2c shows the temperature at the end of the CC discharge for cells with different PFR. The C/20, C/3 and 1 C discharge end temperature are depicted by dark blue circles, bright blue squares, and yellow triangles, respectively. A constant discharge end temperature of roughly 26 °C is measured for all investigated cells with a CC discharge of C/20, all exhibiting a 1 °C increase during the CC C/20 discharge. By applying a CC of C/3 the discharge end temperature varies from roughly 28 °C (high electrolyte cells) to 37 °C (low electrolyte cells), meaning that high electrolyte cells heat up by roughly 3 °C, whereas the low electrolyte cells heat up by 12 °C. When discharging the cells with a CC of 1 C, the discharge end temperature increases further to between 37 °C and 61 °C. Thus, the cells with $PFR_{100} > 1.00$ heat up by 12 °C, whereas the cells with $PFR_{100} \ll 1.00$ heat up by 36 °C. In general, higher currents lead to higher discharge end temperatures, as expected. Furthermore, it is observed that lower electrolyte amounts lead to significantly higher discharge end temperatures.

It is remarkable that even at the very low PFR values investigated (down to $PFR_{100} = 0.62$), the cells retain such high energy output (95.7% at C/3). One contributing factor to the observed lower energy is the loss of the ionic connection of particles, which results in a lower overall capacity. Another factor is an increase of cell resistance, resulting in a reduced average discharge voltage. As the difference in capacity at C/20 between high and low electrolyte cells is less than 3%, this suggests that a reduction of the PFR_{100} to 0.62 results in less than 3% of the particles losing ionic contact, highlighting the surprisingly robust performance of cells with low electrolyte amounts. This nonlinear interdependency between filled pore volume and ionically contacted particles might be explained by a nonlinear wetting of the active material.[31] A possible explanation would be that at a PFR_{100} of 0.62, the pores are not half filled with electrolyte while the other half is completely empty. Rather, due to capillary forces, the particles are coated with a thin film of electrolyte, resulting in a more gradual and uniform distribution of the electrolyte within the porous structure. This strongly depends on the surface properties of the porous active material particles. In hygroscopic materials with pore sizes typically less than 100 nm, a significant portion of the electrolyte is bound to the solid matrix, leading to good wetting of the particle surfaces and the formation of a thin electrolyte film. In contrast, for non-hygroscopic materials with pore sizes typically in the micrometer range (up to 100 μm), the amount of bound electrolyte is negligible, resulting in poorer wetting of the particle surfaces and no significant electrolyte film formation, as shown by Kharaghani et al.[32] In our case, the porous structure of the investigated active material is in the micrometer range. Nevertheless, we assume that the particles themselves have a porous surface structure in the nanometer scale, explaining their good wettability. However, the capacity alone does not fully account for the 4.3% lower C/3 CC discharge energy observed at the lowest PFR compared to the highest PFR, Fig. 2b. The remaining difference can be attributed to the higher resistance at lower PFRs, which will be discussed in more detail in the following sections.

The decreasing energy with increasing C-rates can be explained by the greater overpotential for higher C-rates, which lowers the average voltage and causes the lower cut-off voltage to be reached more rapidly. Thus, at higher C-rates, such as 1 C, we anticipate even lower energies, particularly for cells with low PFR values, compared to lower C-rates. Additionally, higher temperatures are measured for higher C-rates and lower electrolyte amounts. This can be attributed to the overall lower heat capacity and higher resistance for cells with lower electrolyte amounts.[33] Further, with reduced electrolyte volumes, heat dissipation to the steel casing and surrounding environment becomes less efficient. This temperature increase reduces the cell resistance, allowing the cell to deliver more energy. This effect might explain why relatively high energy outputs can still be achieved at 1 C, despite the low electrolyte amount in the lower PFR cells.

The differential voltage (DV) of all investigated cells vs their SoC is shown in Fig. 3. The color scheme represents the PFR_{100}, ranging from low electrolyte content (0.6 PFR_{100}, dark red) to high electrolyte content (1.15 PFR_{100}, dark blue). This color coding is further used throughout this work to visualize the PFR_{100}. The DV is calculated from the CC charge at a low current of C/20, to generate nearly open circuit voltage conditions. The SoC is defined here as the ratio of the capacity charged during the CC C/20 process to the total CC C/20 capacity obtained to investigate the relative peak shift.

The observed peaks in the DV plot correspond to the lithiation phases of the anode and cathode active materials. The minima indicate phase transition regimes where two lithiation phases coexist simultaneously. Based on literature, the individual peaks can be associated with the specific lithiation phases of silicon at low SoC (around 10%), followed by an accumulation of graphite peaks (Gr 1) between 20% and 35% SoC. Subsequently, a NMC peak (NMC 1) is visible around 50% SoC, followed by another graphite peak (Gr 2) at 60% SoC. At approximately 75% SoC, another NMC peak (NMC 2) is observed.[34–36]

The height and position of the NMC 1 and NMC 2 cathode peaks are consistent across all investigated cells. In contrast, the position of the anode peaks Gr 1 and Gr 2 remains constant, but the height decreases and partly vanishes as the PFR decreases. This effect is particularly visible at very low PFRs. This could be explained by an increased inhomogeneity of the lithiation degree within the lithium-ion cell at lower PFRs.[37–40] With decreasing PFR, areas with better-wetted and less-wetted active material arise, leading to locally higher resistances and overpotentials. This results in varying lithiation degrees at different positions inside the cell. Yet, we do not know whether the local inhomogeneities are formed with respect to μm- (individual particles), mm-, or even cm-scale. As the cathode open-circuit potential shows a continuous gradient, different lithiation degrees would result in different local potentials. Hence the lithiation degree within the cathode should balance out quickly, and no effect on the DV is visible. On the other hand, the anode open circuit potential looks like a step function with regions of nearly constant voltage plateaus over a wide range of SoC. Thereby regions with different lithiation degrees can build up while having the same voltage. Once the lithiation degree further increases and a step area with a considerable slope in voltage is reached, a peak in the DVA appears. As varying lithiation degrees have been built up throughout the cell, the lithiation degree cannot be balanced instantaneously. Hence, different voltages appear simultaneously, resulting in a reduced peak height.

In summary, a qualitative visual impact on the DV is observed only for very low PFR values, which we attribute to inhomogeneous

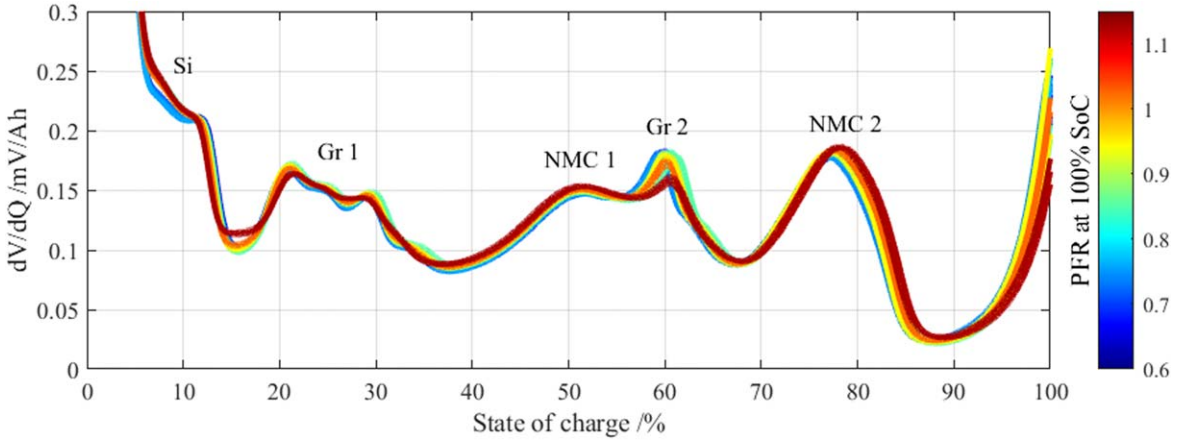

Figure 3. Differential voltage of all investigated cells based on a C/20 charge. The PFR is illustrated by a color scale from dark red (0.6 PFR_{100}) to dark blue (1.15 PFR_{100}). The distinct peaks corresponding to the anode materials (graphite, silicon) and cathode material (NMC) are labeled.

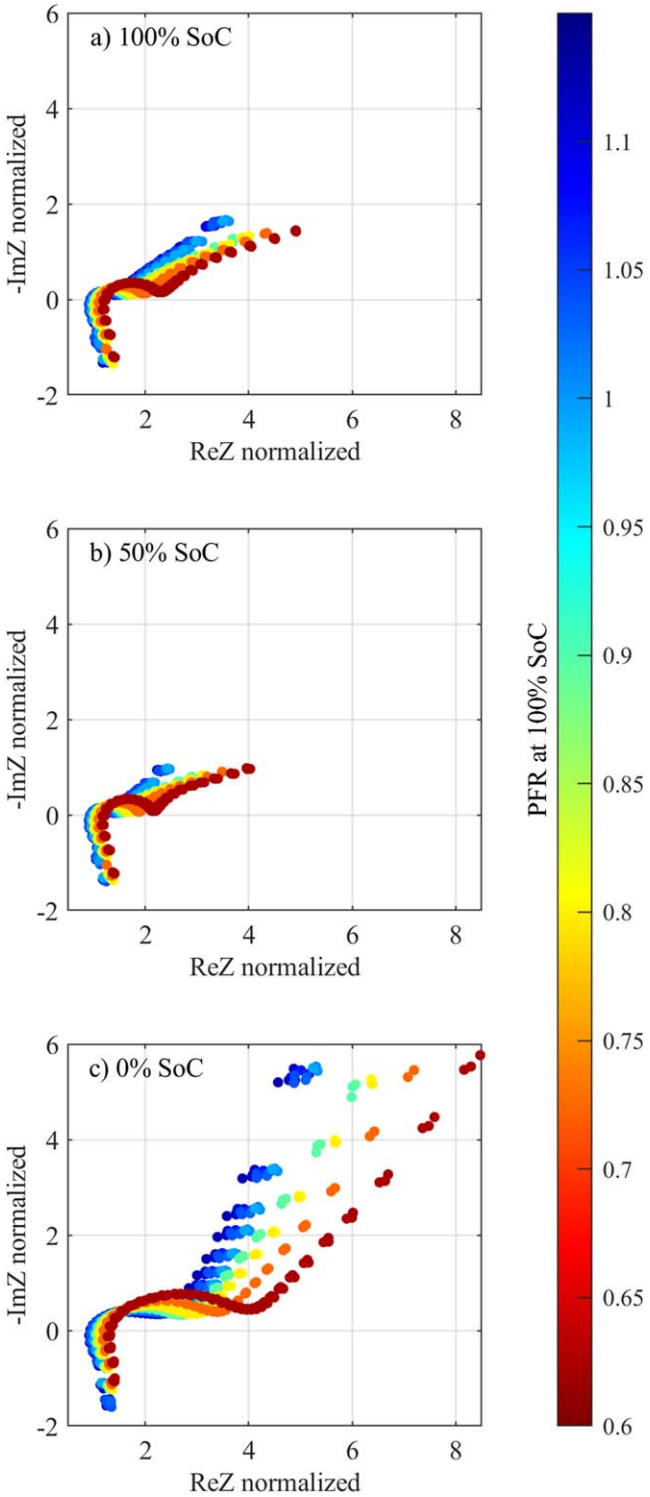

Figure 4. Nyquist plot of investigated cells at (a) 100% SoC, (b) 50% SoC and (c) 0% SoC. The real and imaginary part of the impedance are normalized by the mean of all zero crossing impedances from cells with $PFR_{100} > 1.00$. The color scale illustrates the PFR_{100} from dark red (0.6 PFR_{100}) to dark blue (1.15 PFR_{100}).

lithiation particularly of the anode. As long as the cell is relatively well-wetted, no significant impact of electrolyte amount is observed.

Electrochemical impedance spectroscopy and pulse resistance.—Figure 4 shows the electrochemical impedance spectroscopy (EIS) data for all the investigated cells at (a) 100% SoC, (b) 50% SoC and (c) 0% SoC, represented as Nyquist plots. The impedance values are normalized by the mean high-frequency resistance (HFR) of all cells with PFR values greater than 1.00 across the three SoCs. The HFR represents the real part of the impedance at the intercept at the *x*-axis, where the imaginary part is equal to zero. This point corresponds to a frequency of approximately 1 kHz. All EIS measurements show an inductive branch and one semicircle followed by a linear branch. As the PFR decreases, one can observe a shift of the EIS spectra towards higher real part impedances accompanied by an increase in semicircle width. Further, an overall higher semicircle width is measured at 0% SoC compared to 50% SoC and 100% SoC.

Figure 5 shows the real part of the impedance measured from the galvanostatic EIS as a function of PFR. Note that while the color coding still represents the PFR_{100} of the measured cells, the *x*-axis in Fig. 5 represents the SoC-dependent PFR for the measured cells (see also Table IV). Measurements at 100% SoC, 50% SoC, and 0% SoC are represented by circles, squares, and triangles, respectively. In Fig. 5a the HFR is shown. For cells with PFR $>$ 1.00 (blue data points), the HFR scatters around a constant value. For cells with PFR $=$ 1.00 or smaller (teal to dark red data points), the HFR increases with decreasing PFR. Batch 2 (blue data points) exhibits a greater variation in the HFR compared to batch 1 (teal to dark red data points). This can be attributed to more pronounced fluctuations within the manufacturing process for batch 2, which are also reflected in the greater variation in energy observed in Fig. 2. Within individual cells we observe a remarkably higher HFR at 0% SoC compared to the 50% and 100% SoC, while the latter two exhibit similar values. This splitting of HFR over SoC becomes more pronounced for cells with low PFR. For example, the lowest PFR cell reveals a HFR of 1.35 (0.55 PFR_0) at 0% SoC, 1.22 (0.61 PFR_{50}) at 50% SoC and 1.24 (0.63 PFR_{100}) at 100% SoC, corresponding to a splitting over SoC of 0.11 between 0% and 100% SoC. In constrast, the highest PFR cell shows a HFR of 0.97 (0.99 PFR_0) at 0% SoC, 0.97 (1.09 PFR_{50}) at 50% SoC and 0.96 (1.13 PFR_{100}) at 100% SoC, with only a splitting of 0.01 measured.

The HFR represents the purely ohmic resistance of the cell, which includes the resistance of the electrical connections and wiring, the electrical resistance of the current collectors and the electrode components (active material, conductive additives and binder), and the ionic resistance of the electrolyte located in between anode and cathode inside the separator ($R_{ion,sep}$).[41–43] While the electric resistances are independent of the PFR, $R_{ion,sep}$ is dependent on the PFR: For a PFR equal to one or larger, the separator is well wetted, hence, $R_{ion,sep}$ is constant. With decreasing PFR, the wetting of the separator decreases, whereby $R_{ion,sep}$ and consequently the HFR increases. Further, the HFR is generally independent of SoC, but the observed SoC dependency in cells with low PFR arises from differences in PFR across SoCs. This is clearly visible by an almost constant HFR for all SoCs when the PFR $\geqslant$ 1.00, whereas a strong SoC dependency is measured for cells with PFR $<$ 1.00. Essentially, we can observe the PFR increase with increasing SoC through its influence on the HFR.

Figure 5b investigates the semicircle width, calculated by taking the difference of (i) the minimum between the semicircle and linear branch at around 5 Hz, called low-frequency resistance (LFR), and (ii) the HFR. Hence, the LFR-HFR is located in high to intermediate frequencies $>$ 5 Hz and $<$ 1 kHz. Similar to the HFR, the LFR-HFR is independent on PFR for cells with PFR $>$ 1.00. For cells with PFR $=$ 1.00 or below, the LFR-HFR increases as the PFR decreases. Additionally, the average LFR-HFR measured at 0% SoC is higher compared to 50% SoC and 100% SoC for all cells, independent of PFR.

The LFR-HFR includes the charge transfer resistance of both electrodes (R_{CT}), the SEI resistance and the ionic resistance of the electrolyte inside the electrode pores ($R_{ion,electrode}$).[43–45] Both R_{CT} and $R_{ion,electrode}$ are expected to depend on the PFR regime. As long as the electrode pore volume is completely filled with electrolyte (PFR $\geqslant$ 1.00), R_{CT} and $R_{ion,electrode}$ are independent of the PFR,

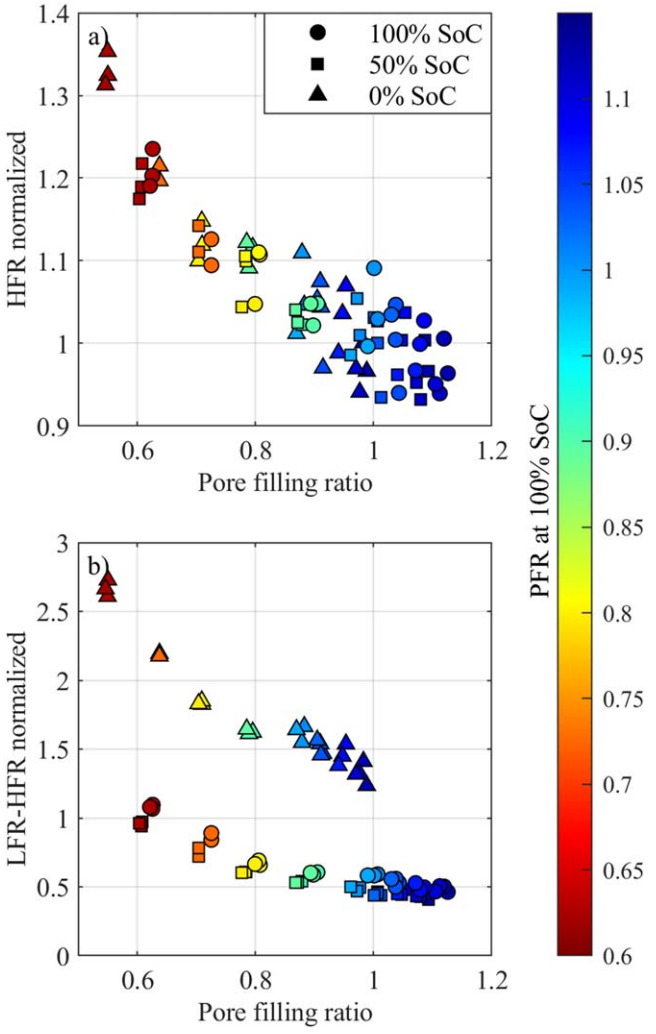

Figure 5. Real part of the impedance measured from galvanostatic EIS vs SoC dependent PFR; (a) high frequency resistance (HFR) and (b) difference between low frequency resistance and high frequency resistance (LFR-HFR). 100% SoC, 50% SoC and 0% SoC are depicted by circles, squares and triangles, respectively. The color scale illustrates the PFR_{100} from dark red (0.6 PFR_{100}) to dark blue (1.15 PFR_{100}).

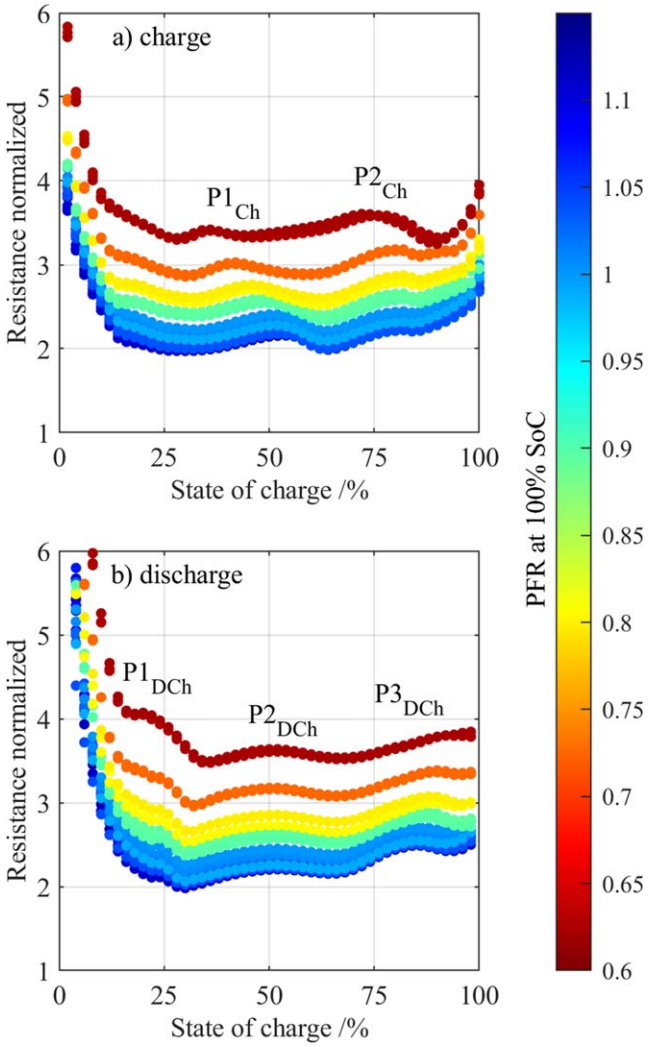

Figure 6. Pulse resistance of all investigated cells evaluated after 10 s in (a) charge and (b) discharge direction vs SoC. The PFR_{100} is illustrated by a color scale from dark red (0.6 PFR_{100}) to dark blue (1.15 PFR_{100}). The two observed peaks in charge direction are marked by $P1_{Ch}$ and $P2_{Ch}$. The three observed peaks in discharge direction are marked by $P1_{DCh}$, $P2_{DCh}$ and $P3_{DCh}$.

resulting in a constant LFR-HFR. As soon as the electrode pore volume is not completely filled anymore (PFR $<$ 1.00), R_{CT} increases, as less active material particles are ionically contacted, resulting in less parallel charge transfer processes and an overall higher R_{CT}. Further, $R_{ion,electrode}$ increases, as the electrode pores are not fully wetted, resulting in a higher effective tortuosity. This results in an overall higher LFR-HFR at low PFR. Additionally, the LFR-HFR reveals a strong SoC dependency, with significantly higher values at 0% SoC compared to 50% and 100% SoC. We attribute this behaviour to the SoC dependency of R_{CT}, which shows higher values at low SoCs due to the high lithiation degree of the cathode.[46,47]

Figure 6 shows the pulse resistance in (a) charge and (b) discharge direction evaluated after 10 s during the rest period and plotted as a function of SoC. To achieve high resolution across the entire SoC range, measurements were performed every 2% SoC. Here, the SoC is defined by the ratio of the charged capacity to the total C/3 discharge capacity for each individual cell. As in Fig. 5, the resistances are normalized by the mean HFR obtained from EIS measurements of all cells with $PFR_{100} > 1.00$ at 0%, 50% and 100% SoC. The data is color coded by PFR_{100} ranging from dark red (0.6 PFR_{100}) to dark blue (1.15 PFR_{100}).

The measured 10 s pulse resistance reveals higher values at both low and high SoCs, which is often described as a "bathtub"-like behavior. In charge direction, two minor peaks at roughly 45% SoC ($P1_{Ch}$) and 80% SoC ($P2_{Ch}$) can be observed, whereas the discharge direction exhibits three peaks at approximately 25% SoC ($P1_{DCh}$), 50% SoC ($P2_{DCh}$) and 85% SoC ($P3_{DCh}$). Note that these peaks do not appear in the 1 s pulse resistance (see supporting information Fig. S2). For $PFR_{100} \geqslant 1.00$, the 10 s pulse resistance shows the same SoC dependency with similar absolute values for all cells in both charge and discharge direction. However, as the PFR_{100} decreases below 1.00, the 10 s pulse resistance increases over the entire SoC range. Comparing cells with the lowest and highest PFR_{100}, the average 10 s pulse resistance difference is 1.3 in charge direction and 1.5 in discharge direction. In discharge direction, the difference in 10 s pulse resistance ranges from ∼1.2 at high SoCs and increases to ∼2.7 at low SoCs. In charge direction, the difference ranges from ∼1.0 at high SoCs to ∼2.0 at low SoCs. Further, the peak $P1_{Ch}$ shifts towards lower SoCs with decreasing PFR_{100}. For example, the highest PFR_{100} cell reaches $P1_{Ch}$ at approximately 50% SoC, whereas the lowest PFR_{100} cell reaches $P1_{Ch}$ at approximately 35% SoC.

The overall increase in the 10 s pulse resistance with decreasing PFR_{100} over the entire SoC range might be explained by a higher $R_{ion,sep}$, R_{CT} and $R_{ion,electrode}$ as previously discussed in detail. At a low PFR, the pores are not completely filled with electrolyte, resulting in a lengthening of the ionic percolation pathway and hence increased resistance. The higher increase in the 10 s pulse resistance at lower SoCs may be related to the lower PFR at low SoCs, increasing the contributions from $R_{ion,sep}$, R_{CT} and $R_{ion,electrode}$.

The observed peaks in charge and discharge direction might arise from changes in diffusion resistance, as these peaks are only evident in the 10 s pulse resistance and not in the 1 s pulse resistance. Based on three-electrode cell pulse measurements (see supporting information Fig. S3), we attribute the peaks mainly to the anode, where they are likely linked to phase transitions in the graphite active material. During charging, silicon and graphite are lithiated in parallel, whereas during discharge, graphite is delithiated first, followed by silicon delithiation. Accordingly, the anode undergoes a hysteresis in expansion and thus also in PFR as graphite expands by 7%–13%, silicon by 280%–311% and NMC contracts by 5%–8% while charging.[24–28,48–50] Consequently, in the charge direction, a continuous anode active material expansion and PFR increase are expected. In the discharge direction, the anode active material remains expanded over a wider SoC range, maintaining a high PFR, before contracting significantly at low SoCs ($< 20\%$), resulting in a sharp PFR decrease. Bond et al.[23] validated this by measuring a hysteresis in free electrolyte (and thus in active material expansion) in 18650 cylindrical cells using in operando synchrotron CT. As silicon and graphite have different resistances at different degrees of lithiation,[51] this might explain the differences in peak positions and overall 10 s pulse resistance values during charge and discharge. At low PFR, we assume less particles are ionically contacted, as previously discussed in Figs. 2a and 2b, which results in higher currents per area and hence faster lithiation of the contacted particles, in contrast to a high PFR cell where the particles are lithiated more homogeneously. Hence, by charging a low PFR cell, phase transitions of graphite might already be reached at lower cell SoC compared to a high PFR cell. This could explain why phase transitions in graphite occur seemingly at lower SoC in low PFR cells, indicated by the shift of the $P1_{Ch}$ peak toward lower SoC.

To summarize the EIS and pulse resistance results, a lower PFR_{100} increases i) the ionic resistance of the electrolyte located inside the separator between the anode and cathode ($R_{ion,sep}$), ii) the ionic resistance of the electrolyte inside the electrode pores ($R_{ion,electrode}$) and iii) the charge transfer resistance (R_{CT}). These effects are only apparent for $PFR_{100} < 1.00$. For cells with $PFR_{100} \geqslant 1.00$ where all pores inside the jelly roll are well-wetted, these resistanceare unaffected by PFR_{100}.

Moment of inertia.—In this study, we elaborate further on the work that has been previously done on the use of MoI measurements to determine and quantify electrolyte motion in cylindrical cells as a function of SoC. Aiken et al. were the first to look at changes in the resonant frequency of the cylindrical cells as a function of charge to qualitatively observe the flow of electrolyte out of the jelly roll and towards the terminal ends of the cells.[18]

The first to use MoI measurements to quantify the mass of electrolyte (in g or mL) moved from the jelly roll were Solchenbach et al. They rearranged Eq. 1 from Aiken et al.[18] which uses the ratio between the MoI at 100% SoC (I_{100}) and the MoI at 0% SoC (I_0) to evaluate the mass of electrolyte moved from the jelly roll into the donut region (see Eq. 3 from Ref. 17). The MoI of the cell is represented by a thin rod. Butler et al.[52] have further developed this equation by modeling the cell using a cylinder and representing the free electrolyte mass located in the donut volume and in the mandrel using additional small cylinders.

In this work we introduce a more precise equation to describe a model for the electrolyte motion in a cylindrical cell. In contrast to the work of Aiken et al.[18] and Solchenbach et al.[17] which used the ratio of I_{100} and I_0 ($\Delta I = I_{100}/I_0$), our approach considers the difference between the MoI at 100% and 0% SoC ($\Delta I = I_{100} - I_0$), as also described by Butler et al.[52] In doing so, all contributions to the MoI from constant mass and volume elements like e.g. the steel can are eliminated. Further, the jelly roll is represented more accurately by the use of a hollow cylinder whose dimensions are dependent on the SoC, whereas Aiken et al.[18] and Solchenbach et al.[17] used a thin rod and Butler et al.[52] a full cylinder to represent the cell, including all cell components, with no SoC dependency. Overall, this means that we only need to analytically describe the components of the cell which may change with SoC, namely the jelly roll dimensions and the distribution of the electrolyte in the cylindrical cell.

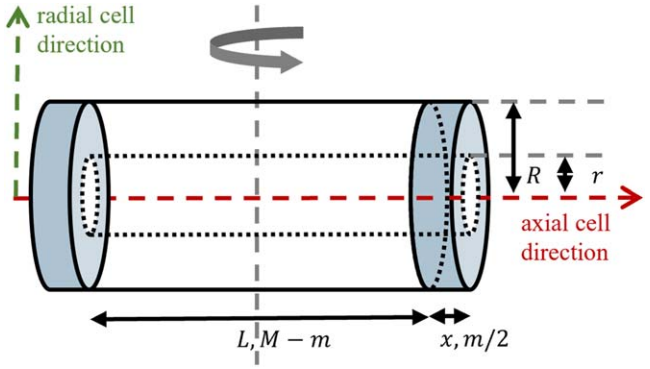

Figure 7. Schematic illustration of a jelly roll rotated through its center of mass of length L, mass M, outer radius R and inner radius r with free electrolyte of mass m and height h located in the donut volume.

The equation considers a cell with $PFR_0 \leqslant 1$, where the electrolyte at 0% SoC is homogeneously distributed through the jelly roll, and no free electrolyte is present. At 100% SoC, the $PFR_{100} > 1$, and free electrolyte is only present in the donut volume. The combined mass of electrolyte and jelly roll solid material is expressed as M. The mass of electrolyte pushed out of the jelly roll is modelled to be distributed equally between the two ends of the donut volume, and is expressed as m. A schematic illustration of the jelly roll with length L outer radius R and inner radius r, and the donut volume of height h is shown in Fig. 7.

The cell is rotated through its center of mass, and the MoI is measured around the central axis labelled in Fig. 7. The reader is referred to the supporting information for the full derivation of the equation, which uses a combination of the MoI formula of a hollow cylinder

$$I = \frac{M}{12} \cdot (3(R^2 + r^2) + L^2) \qquad [4]$$

and the parallel axis theorem to obtain the final analytical Eq. 5 for the MoI change ΔI between 0 and 100% SoC:[30]

$$\begin{aligned}\Delta I = I_{100} - I_0 = {} & \frac{M-m}{12} \cdot [3(R_{100}^2 + r_{100}^2) + L_{100}^2] \\ & - \frac{M}{12} \cdot [3(R_0^2 + r_0^2) + L_0^2] \\ & + \frac{m}{12} \cdot [3(L_{100} + h)^2 + 3(R_{100}^2 + r_{100}^2) + h^2]\end{aligned} \qquad [5]$$

R_0, r_0, L_0 and R_{100}, r_{100}, L_{100} refer to the jelly roll outer diameter, inner diameter and length at 0% SoC and 100% SoC, respectively, obtained by CT-scans. The first and second term in the linear sum relate to the MoI of the jelly roll at 100% and 0% SoC respectively, while the third term describes the contribution to the MoI of the electrolyte m pushed into the donut volume.

Compared to previous approaches for determining the mass of electrolyte moved from MoI measurements,[17] this model provides a significant advancement by accounting for the changes occurring

within the jelly roll as a function of SoC. This enables the isolation of the contributions to MoI exclusively from electrolyte motion within the cell, as demonstrated in the discussion section below. It is important for the reader to note that the MoI technique, and our analytical model, both have their limitations. The MoI measurement is only sensitive to motion of the electrolyte in the axial direction of the cell (as labelled in Fig. 7). Electrolyte motion occurring in the radial direction will not be probed by this experimental technique.

The analytical model itself relies on assumptions, which impose limitations on its applicability. Firstly, we assume a linear correspondence between the MoI increase and the amount of electrolyte being pushed into the donut volume. This assumption holds only if the electrolyte remains homogeneously distributed within the jelly roll across all SoCs. Additionally, as extensively discussed by Aiken et al., the correlation between MoI changes and electrolyte mass moved to the terminals of the cell is valid only if the displaced electrolyte is fully confined within the donut volume, which is not the case for cells with significant electrolyte overflow into the hollow core ($PFR_{100} \gg 1$). Consequently, the model is most applicable to cells with $PRF_0 \leqslant 1.00$ and $PFR_{100} > 1.00$, provided that the displaced electrolyte remains within the donut region.

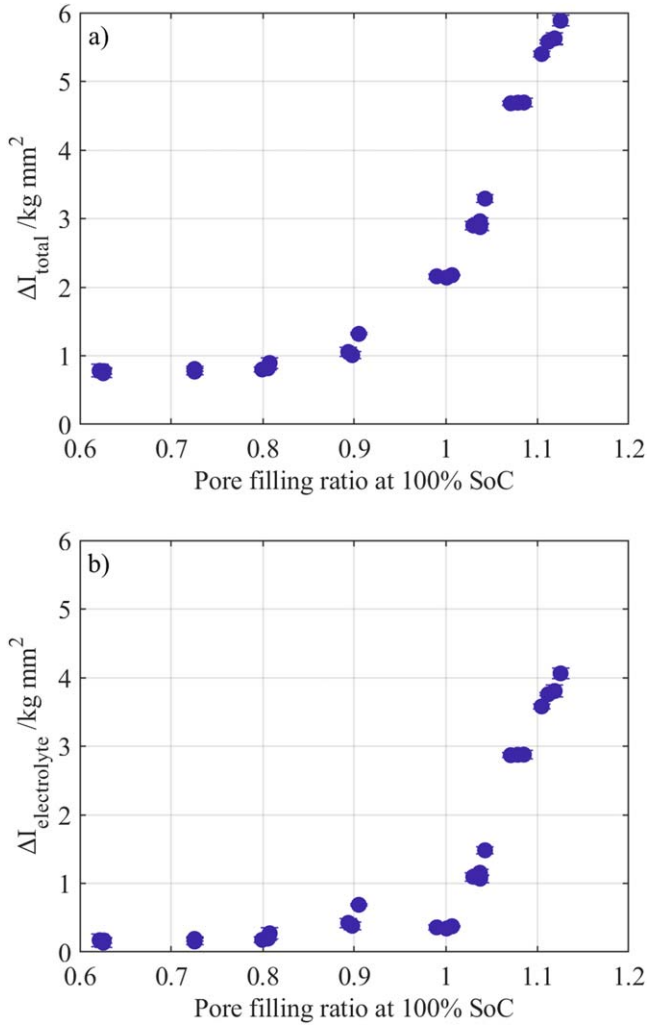

Figure 8. The difference in moment of inertia between 100% SoC and 0% SoC (ΔI) is plotted against the PFR at 100% SoC for all investigated cells. Error bars indicate the maximum and minimum measured values of the two consecutive measurements. (a) Shows the total measured ΔI_{total}. In (b) $\Delta I_{electrolyte}$ only represents the contribution from electrolyte motion, obtained by subtracting the ΔI resulting from jelly roll expansion from the total measured ΔI_{total}.

Figure 8a illustrates the relationship between the total measured moment of inertia change (ΔI_{total}) during a full state-of-charge cycle (0% SoC to 100% SoC) and the PFR_{100} of all investigated cells. Here, we first want to analyze the measured moment of inertia in detail. In the following discussion, we will focus on the physically relevant quantity, the displaced electrolyte volume. An increase in MoI indicates the movement of mass from the center of the cell towards the terminal ends, along the axial direction labelled in Fig. 7. For $PFR_{100} < 1.00$, ΔI_{total} remains approximately constant, with an average value of 0.89 kg mm^2. At $PFR_{100} = 1.00$, ΔI_{total} increases to a mean value of 2.16 kg mm^2. Beyond $PFR_{100} > 1.00$, ΔI_{total} increases linearly with increasing PFR_{100}.

The MoI change is sensitive to all mass moved along the axial direction of the cell. The CT-scans of the cells at 100% SoC show a lengthening of the jelly roll (see L_0 and L_{100} in Table III), which will result in an increase of the MoI of the cell additional to any electrolyte movement. It is therefore useful to isolate the contribution to the MoI change of the jelly roll expansion from the MoI change caused by electrolyte motion alone, $\Delta I_{electrolyte}$. Figure 8b presents the MoI change solely attributed to electrolyte redistribution. This is derived by subtracting the contribution of jelly roll length expansion ($\Delta I_{jelly\ roll}$) from the total ΔI_{total}. The contribution from jelly roll expansion is calculated using Eq. 5, along with the mean jelly roll dimensions at 0% and 100% SoC for cell batches 1 and 2, yielding 0.62 kg mm^2 for batch 1 and 1.81 kg mm^2 for batch 2. Below $PFR_{100} = 1.00$, $\Delta I_{electrolyte}$ remains near zero, with an average value of 0.27 kg mm^2. At $PFR_{100} = 1.00$, $\Delta I_{electrolyte}$ increases slightly to an average of 0.36 kg mm^2. For $PFR_{100} > 1.00$, $\Delta I_{electrolyte}$ exhibits a linear increase with rising PFR_{100} up to 4.06 kg mm^2. For $PFR_{100} < 1.00$, we do not expect the generation of free electrolyte, consistent with the experimentally observed $\Delta I_{electrolyte}$, which is close to zero. $PFR_{100} = 1.00$ marks the onset of electrolyte expulsion from the jelly roll, and the measured $\Delta I_{electrolyte}$ increases suddenly, reflecting this behaviour. As PFR_{100} increases above 1.00, more free electrolyte is pushed into the donut volume, leading to a linear increase in $\Delta I_{electrolyte}$, in agreement with our predictions for the cells.

These results provide direct evidence of a correlation between the change in MoI and the expected extent of free electrolyte generation during cycling, with a clear transition at $PFR_{100} = 1.00$. This finding highlights MoI as an outstanding measurement method to determine the inflection point when significant amounts of free electrolyte are generated at 100% SoC.

Discussion

Electric performance.—Within this study, we have found that for cells with a $PFR_{100} > 1.00$, where the anode, cathode and separator are completely filled with electrolyte, the energy as well as the resistance are independent of the PFR. Additional free electrolyte located outside the jelly roll neither improves nor degrades the electric performance. As soon as the PFR_{100} falls below 1.00, the pore volume in the anode, cathode, and separator is not completely filled with electrolyte, meaning that the energy decreases and the resistance increases with decreasing PFR, as the tortuosity increases and the amount of ionically contacted particles decreases.

Günter et al.[2] and An et al.[3] also found that above a certain PFR threshold, the specific capacity, resistance, and consequently electrical performance become independent of a further increase in the PFR. Conversely, when the PFR drops below this threshold, capacity and energy decrease, and the resistance increases. In contrast to our findings, they did not specifically locate this performance transition at a PFR = 1.00. Günter et al.[2] found this transition point at a PFR = 1.4, while An et al.[3] examined it at an even higher value of PFR = 2.1.

It is important to note that Günter et al.[2] and An et al.[3] investigated pouch cells and defined the PFR by a simplified model based on the filled electrolyte volume and the pore volume of pristine separator, cathode and anode sheets. In this paper, however,

the PFR is referring to the electrolyte amount and pore volume in the assembled cell after formation. Thereby, Günter et al.[2] and An et al.[3] do not take into account an initial swelling of the electrodes during formation resulting in a different pore volume.[20,21] Further, the initial SEI formation leading to electrolyte and pore volume loss is not considered. Hence, to enable a valid comparison between the different studies, the PFR has to be defined uniformly.

Additionally, small-format pouch cells have a higher ratio of empty volume to jelly roll volume compared to large-format cylindrical cells. Hence, within smaller pouch cells, more relative space is available for the electrolyte to be located outside the jelly roll. Thus, these pouch cells might show a different electrolyte distribution compared to cylindrical cells. A theoretical PFR of 1.00 in pouch cells might therefore not be equal to a completely filled pore volume, whereas in the investigated cylindrical cells, a PFR of 1.00 most likely corresponds to a completely filled pore volume, as evident from the electrical tests and the moment of inertia results.

Free electrolyte volume.—In this section the robustness of Eq. 5, developed for the analysis of the MoI, is investigated. To do this, Eq. 5 is used to transform the MoI changes into a more intuitive metric: the volume of free electrolyte expelled from the jelly roll into the donut volume during charging from 0% to 100% SoC. Then, the volume of free electrolyte predicted by the experimentally obtained MoI changes ($V_{\text{free electrolyte; MoI}}$) is compared to the volume of free electrolyte expected from the PFR calculations ($V_{\text{free electrolyte; PFR}}$). These two techniques are independent from each other, the $V_{\text{free electrolyte; PFR}}$ is a result of a theoretical prediction based on our models of the cells, while $V_{\text{free electrolyte; MoI}}$ is derived from experimental measurements.

The $V_{\text{free electrolyte; PFR}}$ is defined as the difference between the total electrolyte volume $V_{\text{electrolyte}}$ present in the cell and the pore volume V_{pore} available within the jelly roll, calculated from Eq. 2:

$$V_{\text{free electrolyte; PFR}} = V_{\text{electrolyte}} - V_{\text{pore}}(100\%\ \text{SoC}) \quad [6]$$

This value gives an estimate of the possible amount of electrolyte that is pushed out from the jelly roll at 100% SoC when $\text{PFR}_{100} > 1.00$. For $\text{PFR}_{100} < 1.00$, the pore volume in the jelly roll is sufficient to accommodate the entire electrolyte volume, resulting in $V_{\text{free electrolyte; PFR}} = 0$.

The experimentally measured $V_{\text{free electrolyte; MoI}}$ at 100% SoC is obtained by combining the free electrolyte mass $m_{\text{free electrolyte}}$ determined from ΔI_{total} (see Eq. 5) with the electrolyte density. The calculation of $m_{\text{free electrolyte}}$ was performed using the average jelly roll dimensions R_{100}, r_{100}, L_{100}, R_0, r_0, L_0 obtained from CT-scans for cell batches 1 and 2. CT-scans were used to confirm the lack of electrolyte overflow into the mandrel, and thus to justify the use of our model. The free electrolyte volume in the donut region is estimated using the height of the electrolyte column (h), corresponding to one-third of the donut height, based on CT-imaging.

Figure 9 illustrates $V_{\text{free electrolyte; MoI}}$ (dark blue dots) and $V_{\text{free electrolyte; PFR}}$ (light blue dots) at 100% SoC for all investigated cells as a function of PFR_{100}. Overall, both predictions agree well with an equal trend and the same order of magnitude of the free electrolyte volume. For $\text{PFR}_{100} < 1.00$, both calculated and measured free electrolyte volumes are effectively zero. For $\text{PFR}_{100} > 1.00$, both volumes increase linearly with increasing PFR_{100}, but with slightly different slopes, resulting in a divergence between theoretical $V_{\text{free electrolyte; PFR}}$ and experimental $V_{\text{free electrolyte; MoI}}$ values. While the MoI measurement underestimates the amount of free electrolyte, the PFR calculation overestimates the amount of free electrolyte. The calculated amount of free electrolyte increases to 4.3 ml at the highest PFR, whereas the experimentally determined amount of free electrolyte only reaches a value of 2.7 ml, resulting in a discrepancy of 1.6 ml.

This discrepancy between the $V_{\text{free electrolyte; MoI}}$ and $V_{\text{free electrolyte; PFR}}$, can be better understood if we consider the limitations of the MoI measurement and the PFR calculations. As

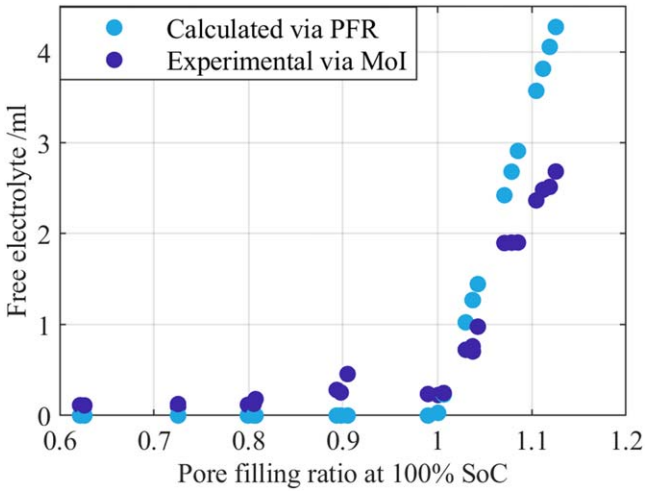

Figure 9. Free electrolyte volume plotted against the PFR_{100}. Experimentally measured free electrolyte volume based on MoI change between 0% SoC and 100% SoC and calculated free electrolyte volume based on the pore filling ratio model are shown in dark blue and light blue, respectively.

previously mentioned, the technique does not capture electrolyte motion in the radial direction within the cell but can only estimate electrolyte motion in the axial direction, into the donut volume. In cells with significant excess of free electrolyte, Bond et al.[23] observed films of electrolyte coating the mandrel. This is thought to be due to electrolyte adhering to the porous separator and external jelly roll surfaces via capillary forces. Very small electrolyte films would probably not be visible in our CT-scans, and since it is the result of a net motion along the radial cell direction, it would also not be visible in the MoI measurements.

This is thought to be due to electrolyte adhering to the outermost layer of the porous separator and the external jelly roll surfaces via capillary forces. Such thin electrolyte films, which could also grow and shrink during charge and discharge, would not be visible in our CT-scans but could result in a net electrolyte motion along the radial cell direction, which thus would not be detected by the MoI measurements. Accordingly, the MoI measurement indicates the lower boundary of the generated free electrolyte. Further, the PFR calculations are also based on assumptions (i.e., regarding electrolyte consumption during formation) and do not necessarily represent the ground truth. Thus, it is possible that the PFR calculation slightly overestimates the amount of free electrolyte. Overall, the PFR calculations align well with the transition point from “no free” to “free” electrolyte that was found by MoI measurements and also visible in the electrical tests.

To estimate the effect of the potential error on $V_{\text{free electrolyte; MoI}}$, the volumes of thin electrolyte films covering the outer and inner jelly roll are calculated using the formula of a hollow cylinder. The outer film volume is determined using the jelly roll dimensions at 100% SoC and a film thickness of 0.06 mm, as estimated from CT-imaging as the gap between the jelly roll and the inner wall of the cell can. For the mandrel, an analogous film thickness was assumed to be 0.5 mm (∼10% of the mandrel diameter). The combination of these thicknesses yields an estimated total electrolyte film volume of 1.2 ml. This would result in the presence of an additional 1.2 ml of generated free electrolyte at 100% SoC, which cannot be probed with our MoI experiments. This amount is in the same range as the maximum measured discrepancy between $V_{\text{free electrolyte; MoI}}$ and $V_{\text{free electrolyte; PFR}}$ at the highest investigated PFR, namely1.6 ml. Accordingly, we want to show that the deviations between theoretical and measured free electrolyte volumes can be well explained by thin film formations. Nevertheless, there are also other influencing factors that contribute to the deviation, such as deviations in the

exact free electrolyte volume due to the PFR calculation, as discussed above.

Summarized, we have verified the robustness of our analytical model when predicting the mass of free electrolyte generated in cell with $PFR_0 \leqslant 1.00$ and $PFR_{100} > 1.00$. While an experimental technique that can determine the exact PFR as a function of cell aging is yet to be found, we demonstrate the applicability of the MoI method as a technique to corroborate PFR calculations and distinguish the onset of free electrolyte generation.

Conclusions

This study explores the impact of electrolyte quantity on the electrochemical performance of high-energy cylindrical lithium-ion batteries at the beginning of life. The analyzed cells are prototype 4695 cells produced at BMW facilities consisting of high nickel NMC cathode active material and a composition of Gr and Si as anode active material. Their pore filling ratio at 100% SoC (PFR_{100}) ranges from roughly half-filled jelly roll pore volume of 0.62 to completely filled with additional free electrolyte ($PFR_{100} = 1.12$). As long as the PFR exceeds 1.00, the energy and resistance remain constant. In general, the energy decreases with decreasing PFR, due to capacity losses and resistance rise. Still, the C/3 discharge energy of cells with a very low PFR_{100} of 0.62 reveals surprisingly high energies, reaching 96% of the energy of cells with a PFR_{100} greater than or equal to 1.00. Despite only approximately half of the free pore volume being filled with electrolyte, the majority of the active material particles still appear to be ionically accessible, which might be explained by a nonlinear wetting of the active material. Additionally, for very low PFR_{100}, the differential voltage analysis shows decreasing anode peak heights, which we attribute to an increased inhomogeneity in the lithiation degree due to an inhomogeneous wetting of the active materials.

Electrochemical impedance spectroscopy (EIS) and pulse measurements are performed to analyze the resistance in detail. By investigating the zero crossing of the EIS, an increased ohmic resistance with decreasing PFR is observed as soon as the PFR_{100} drops below 1.00. This can be attributed to an increased ionic resistance of the electrolyte located between anode and cathode inside the separator with decreasing PFR. Additionally, the semicircle width increases with decreasing PFR as soon as the PFR_{100} drops below 1.00. Since less active material area is wetted with a low PFR, fewer parallel charge transfer reactions can take place, resulting in an overall higher charge transfer resistance. Further, the lower wetting results in a higher tortuosity and hence increased ionic resistance of the electrolyte inside the electrode pores. Pulses measured with high resolution every 2% SoC reveal minor peaks probably attributed to diffusion resistance changes within the graphite active material during phase transition. Peak $P1_{Ch}$ present at low SoCs, while charging, is shifted to even lower SoC values as the PFR decreases. This behavior might be related to higher currents per area at low PFR resulting in an inhomogeneous lithiation degree.

We expand on the use of the moment of inertia (MoI) technique as a powerful, non-destructive method for probing electrolyte dynamics in cylindrical lithium-ion cells. In this work we develop an analytical framework which enables the prediction of free electrolyte pushed into the donut volume during charging from 0% to 100% SoC. By analysing the difference in MoI between 100% SoC and 0% SoC, we can uncouple the effects of jelly roll expansion and electrolyte redistribution. For cells with $PFR_{100} < 1$, no electrolyte is displaced outside the jelly roll, resulting in negligible MoI change. However, once the PFR_{100} exceeds 1.00, free electrolyte is expelled, leading to a linear increase in MoI change with increasing PFR.

This study highlights that MoI measurements can reliably determine whether a cell exhibits free electrolyte ($PFR > 1.00$) or not ($PFR \leqslant 1.00$) and help estimate the volume of free electrolyte displaced during charging. Despite limitations, such as sensitivity only to axial electrolyte motion and assumptions of uniform distribution, the technique demonstrates excellent agreement with theoretical expectations from PFR calculations, making it a valuable tool for understanding electrolyte dynamics and their impact on cell performance.

We have developed a thorough analysis protocol to probe the electrical performance of cylindrical cells, and to non-destructively probe electrolyte dynamics. While the findings presented here can be universally adopted, for newly investigated cells, the specific geometry and characteristics of the electrodes used must be considered. The drawn framework will be applied in a subsequent study to analyse the effects of electrolyte filling on the aging of cylindrical cells.

Acknowledgments

The authors want to thank Daniel Pritzel, David Bemmerl, Lea Wallisch, Anna Stanke, Cornelius Hupbauer, Jonas Kayl, Volker Winkler, and Matthias Füchsl (all BMW AG) for their support with cell assembly, CT-scan analysis, and moment of inertia measurements.

Further we want to thank Zheng Li and Sebastian Salzinger (Capgemini Deutschland GmbH, Germany) for performing the electrical tests.

ORCID

Cara Zimmermann https://orcid.org/0009-0005-2706-4121
Camilla Tacconis https://orcid.org/0000-0003-1128-1023
Sophie Solchenbach https://orcid.org/0000-0001-6517-8094
Daniel Goldbach https://orcid.org/0009-0009-0230-4482
Simon Erhard https://orcid.org/0000-0002-5029-7477
Johannes Wandt https://orcid.org/0000-0003-4615-9618
Simon Lux https://orcid.org/0009-0001-5825-3516

References

1. R. Schmuch, R. Wagner, G. Hörpel, T. Placke, and M. Winter, *Nat. Energy*, **3**, 267 (2018).
2. F. J. Günter, C. Burgstaller, F. Konwitschny, and G. Reinhart, *J. Electrochem. Soc.*, **166**, A1709 (2019).
3. S. J. An et al., *ACS Appl. Mater. Interfaces*, **9**, 18799 (2017).
4. S. J. An et al., *J. Electrochem. Soc.*, **164**, A1195 (2017).
5. R. Gauthier et al., *J. Electrochem. Soc.*, **169**, 020518 (2022).
6. D. A. Stevens et al., *J. Electrochem. Soc.*, **161**, A1364 (2014).
7. J. Park et al., *J. Power Sources*, **365**, 257 (2017).
8. J. Sieg et al., *Appl. Energy*, **305**, 117747 (2022).
9. M. J. Mühlbauer, O. Dolotko, M. Hofmann, H. Ehrenberg, and A. Senyshyn, *J. Power Sources*, **348**, 145 (2017).
10. L. M. Thompson et al., *J. Electrochem. Soc.*, **165**, A2732 (2018).
11. R. Jung et al., *J. Electrochem. Soc.*, **163**, A1705 (2016).
12. P. M. Attia et al., *J. Electrochem. Soc.*, **169**, 060517 (2022).
13. R. Petibon et al., *J. Electrochem. Soc.*, **161**, A1167 (2014).
14. R. Stockhausen et al., *J. Electrochem. Soc.*, **168**, 080504 (2021).
15. Z. Deng et al., *Joule*, **4**, 2017 (2020).
16. S. Schönemeier, V. Peters, F. Horsthemke, H. Seo, and F.-M. Matysik, *Anal. Chim. Acta*, **1336**, 343530 (2025).
17. S. Solchenbach et al., *Energy Environ. Sci.*, **17**, 7294 (2024).
18. C. P. Aiken et al., *J. Electrochem. Soc.*, **170**, 040529 (2023).
19. M. Ank et al., *J. Electrochem. Soc.*, **170**, 120536 (2023).
20. F. B. Spingler, S. Kücher, R. Phillips, E. Moyassari, and A. Jossen, *J. Electrochem. Soc.*, **168**, 040515 (2021).
21. T. Deich, S. L. Hahn, S. Both, K. P. Birke, and A. Bund, *Journal of Energy Storage*, **28**, 101192 (2020).
22. N. S. Nazer, M. Strobl, A. Kaestner, P. J. S. Vie, and V. A. Yartys, *Electrochim. Acta*, **427**, 140793 (2022).
23. T. Bond et al., *J. Electrochem. Soc.*, **172**, 030512 (2025).
24. A. J. Louli, J. Li, S. Trussler, C. R. Fell, and J. R. Dahn, *J. Electrochem. Soc.*, **164**, A2689 (2017).
25. B. Rieger et al., *Journal of Energy Storage*, **6**, 213 (2016).
26. S. Schweidler et al., *J. Phys. Chem. C*, **122**, 8829 (2018).
27. X. H. Liu et al., *Nature Nanotech*, **7**, 749 (2012).
28. L. Y. Beaulieu, T. D. Hatchard, A. Bonakdarpour, M. D. Fleischauer, and J. R. Dahn, *J. Electrochem. Soc.*, **150**, A1457 (2003).
29. A. Durdel et al., *J. Electrochem. Soc.*, **172**, 050508 (2025).
30. W. Demtröder, *Experimentalphysik 1: Mechanik und Wärme* (Springer Berlin Heidelberg, Berlin, Heidelberg) (2021).
31. C. Kupper, B. Weißhar, S. Rißmann, and W. G. Bessler, *J. Electrochem. Soc.*, **165**, A3468 (2018).

32. A. Kharaghani, "Drying and Wetting of Capillary Porous Materials: Insights from Imaging and Physics-based Modeling." *Doctoral dissertation*, Fakultaet fur Verfahrens- und Systemtechnik ¨ der Otto-von-Guericke-Universit¨at Magdeburg (2020).
33. H. Maleki, S. A. Hallaj, J. R. Selman, R. B. Dinwiddie, and H. Wang, *J. Electrochem. Soc.*, **146**, 947 (1999).
34. J. Sturm et al., *J. Power Sources*, **412**, 204 (2019).
35. J. Schmitt, M. Schindler, A. Oberbauer, and A. Jossen, *J. Power Sources*, **532**, 231296 (2022).
36. P. Keil and A. Jossen, *J. Electrochem. Soc.*, **164**, A6066 (2017).
37. M. Lewerenz, A. Marongiu, A. Warnecke, and D. U. Sauer, *J. Power Sources*, **368**, 57 (2017).
38. D. Beck, P. Dechent, M. Junker, D. U. Sauer, and M. Dubarry, *Energies*, **14**, 3276 (2021).
39. J. P. Fath et al., *Journal of Energy Storage*, **25**, 100813 (2019).
40. M. Dubarry and B. Y. Liaw, *J. Power Sources*, **194**, 541 (2009).
41. W. Choi, H.-C. Shin, J. M. Kim, J.-Y. Choi, and W.-S. Yoon, *J. Electrochem. Sci. Technol*, **11**, 1 (2020).
42. N. Meddings et al., *J. Power Sources*, **480**, 228742 (2020).
43. N. Ogihara et al., *J. Electrochem. Soc.*, **159**, A1034 (2012).
44. S. Solchenbach, X. Huang, D. Pritzl, J. Landesfeind, and H. A. Gasteiger, *J. Electrochem. Soc.*, **168**, 110503 (2021).
45. P. Iurilli, C. Brivio, and V. Wood, *J. Power Sources*, **505**, 229860 (2021).
46. S. Gantenbein, M. Weiss, and E. Ivers-Tiffée, *J. Power Sources*, **379**, 317 (2018).
47. M. Koseoglou et al., *Journal of Energy Storage*, **73**, 109051 (2023).
48. J. Knorr et al., *J. Electrochem. Soc.*, **171**, 080512 (2024).
49. F. Friedrich et al., *J. Electrochem. Soc.*, **166**, A3760 (2019).
50. L. D. Biasi et al., *J. Phys. Chem. C*, **121**, 26163 (2017).
51. J. Knorr et al., *Journal of Energy Storage*, **86**, 111151 (2024).
52. E. J. Butler et al., *Meet. Abstr.*, **MA2024-02**, 414 (2024).